NASA/TM—2019-220045 AIAA–2019–2588

Transfer-Function Determination for Infinite-Tube-Probe Pressure Transducers With Application to Turbofan Core/Combustor Noise

Devin K. Boyle, Brenda S. Henderson, and Lennart S. Hultgren
Glenn Research Center, Cleveland, Ohio

June 2019

NASA STI Program . . . in Profile

Since its founding, NASA has been dedicated to the advancement of aeronautics and space science. The NASA Scientific and Technical Information (STI) Program plays a key part in helping NASA maintain this important role.

The NASA STI Program operates under the auspices of the Agency Chief Information Officer. It collects, organizes, provides for archiving, and disseminates NASA's STI. The NASA STI Program provides access to the NASA Technical Report Server—Registered (NTRS Reg) and NASA Technical Report Server—Public (NTRS) thus providing one of the largest collections of aeronautical and space science STI in the world. Results are published in both non-NASA channels and by NASA in the NASA STI Report Series, which includes the following report types:

- TECHNICAL PUBLICATION. Reports of completed research or a major significant phase of research that present the results of NASA programs and include extensive data or theoretical analysis. Includes compilations of significant scientific and technical data and information deemed to be of continuing reference value. NASA counter-part of peer-reviewed formal professional papers, but has less stringent limitations on manuscript length and extent of graphic presentations.

- TECHNICAL MEMORANDUM. Scientific and technical findings that are preliminary or of specialized interest, e.g., "quick-release" reports, working papers, and bibliographies that contain minimal annotation. Does not contain extensive analysis.

- CONTRACTOR REPORT. Scientific and technical findings by NASA-sponsored contractors and grantees.

- CONFERENCE PUBLICATION. Collected papers from scientific and technical conferences, symposia, seminars, or other meetings sponsored or co-sponsored by NASA.

- SPECIAL PUBLICATION. Scientific, technical, or historical information from NASA programs, projects, and missions, often concerned with subjects having substantial public interest.

- TECHNICAL TRANSLATION. English-language translations of foreign scientific and technical material pertinent to NASA's mission.

For more information about the NASA STI program, see the following:

- Access the NASA STI program home page at http://www.sti.nasa.gov

- E-mail your question to help@sti.nasa.gov

- Fax your question to the NASA STI Information Desk at 757-864-6500

- Telephone the NASA STI Information Desk at 757-864-9658

- Write to:
  NASA STI Program
  Mail Stop 148
  NASA Langley Research Center
  Hampton, VA 23681-2199

NASA/TM—2019-220045 AIAA–2019–2588

Transfer-Function Determination for Infinite-Tube-Probe Pressure Transducers With Application to Turbofan Core/Combustor Noise

Devin K. Boyle, Brenda S. Henderson, and Lennart S. Hultgren
Glenn Research Center, Cleveland, Ohio

Prepared for the
25th AIAA/CEAS Aeroacoustics Conference
cosponsored by the American Institute of Aeronautics and Astronautics (AIAA)/Council of European Aerospace Societies (CEAS)
Delft, The Netherlands, May 20–23, 2019

National Aeronautics and
Space Administration

Glenn Research Center
Cleveland, Ohio 44135

June 2019

Acknowledgments

Drs. Bill Schuster and Duane McCormick are thanked for helpful discussions and advice.

This work was sponsored by the Advanced Air Vehicle Program
at the NASA Glenn Research Center

Level of Review: This material has been technically reviewed by technical management.

Available from

NASA STI Program
Mail Stop 148
NASA Langley Research Center
Hampton, VA 23681-2199

National Technical Information Service
5285 Port Royal Road
Springfield, VA 22161
703-605-6000

This report is available in electronic form at http://www.sti.nasa.gov/ and http://ntrs.nasa.gov/

Transfer-Function Determination for Infinite-Tube-Probe Pressure Transducers With Application to Turbofan Core/Combustor Noise

Devin K. Boyle, Brenda S. Henderson, and Lennart S. Hultgren
National Aeronautics and Space Administration
Glenn Research Center
Cleveland, Ohio 44135

Abstract

Turbofan hot-section unsteady pressure measurements are complicated by environmental limitations of current-generation sensors. Accurate direct measurements are normally not possible and engine-external measurement techniques, using sufficiently long sense lines, are utilized instead. Remote measurement comes at a cost, however, as it introduces a magnitude reduction within the line as well as a phase lag relative to the desired engine-internal measurement location. Determination, or validation, of a transfer function relating the engine-internal pressure to the observed remote value is necessary. Transfer functions are examined for various configurations of the so-called infinite-tube-probe arrangement in order to optimize measurement performance. The experimental setup uses a normal-incidence tube that ordinarily is utilized for impedance eduction. Here, its downstream end instead is made up of a hard-wall termination instrumented with a flush-mounted microphone and a Kulite® pressure transducer as well as a sense line connection. This allows the remote and direct measurements to be related under controlled conditions. Transfer-function measurements are presented and compared to predictions for several parametric variations.

I. Introduction

The current turbofan-engine design trends [1] of lean-burning combustors and smaller high-pressure-ratio cores in combination with lower-blade-count, wide-chord-blade turbines and lower-jet-exhaust velocities, are expected to make core/combustor noise a more prominent propulsion-noise source in the future [2, 3]. Consequently, a better understanding of the source mechanism(s) of combustor noise is imperative. This can ultimately only be achieved by utilizing advanced source-separation techniques [4–9] that often combine engine-internal measurements with farfield acoustic measurements. Such source-separation methods are needed because combustor noise is normally masked by jet noise under static-engine-test conditions due to the absence of forward-flight effects. Engine hot-section unsteady pressure measurements are also useful for a variety of other applications such as thermo-acoustic-instability control, etc.

Direct measurement of unsteady pressures within the core of a turbofan engine is often impossible due to the extreme environment (high-temperature, high-pressure). Consequently, pressure transducers are mounted externally and coupled to the desired measurement location with a sufficiently long waveguide. However, this sense line introduces both a magnitude drop and a phase lag relative to the unsteady pressure at the intended measurement location inside the core. In addition, reflections from the waveguide termination can lead to standing-wave resonances that degrade the measurement capability. For this reason, the waveguide is commonly continued past the pressure transducer for a sufficiently long distance such that reflected pressure fluctuations are attenuated through dissipation well before reaching the transducer location. The 'infinite' line segment is normally much longer than the sense line (between the probe tip and the transducer). This arrangement is commonly referred to as the infinite-tube-probe (ITP) configuration, or sometimes as the semi-infinite-tube configuration. The former nomenclature, rather than the latter, will be used herein.

The remote measurement approach utilizing an ITP is a reasonably well-established method for measurement under conditions that the transducers cannot directly tolerate [10, 11]. However, the experimental determination/validation of a transfer function relating the desired unsteady pressure to the ITP-transducer measured value is necessary, particularly if the instrumentation layout requires a long sense line or if higher frequencies (say, a couple of kHz) are considered important. Transfer functions are examined herein for various ITP configurations in order to optimize measurement performance under design constraints relevant to engine tests.

The outline of the paper is as follows: The experimental setup is described in Section II; a formula for the transfer function, using existing theory [12–14], is discussed in Section III, with more details given in Appendices A and B; the results are described in Section IV; and finally, Section V offers a summary, conclusions, and recommendations.

II. Experimental Setup

The experiment is performed using a simple modification of an existing normal-incidence tube (NIT) at NASA Glenn Research Center (GRC). The NIT's 2 inch × 2 inch (50.8 mm × 50.8 mm) square cross section and acoustic driver offer a useful frequency range of approximately 500 Hz to 3 kHz. Instead of a holder for a sample liner (whose impedance characteristics are of interest), the tube is fitted with a modified hard-wall termination containing a flush-mounted 1/4-inch GRAS front-vented pressure-field microphone (Model 46BD-FV), a flush-mounted Kulite® high-sensitivity 10 psid pressure transducer (XCS-190S-10D) and an ITP sense-line connector. The ITP uses an identical type Kulite® transducer. Figure 1 shows the entire NIT from speaker (left) to termination (right) and Fig. 2 shows the termination of the tube in more detail. Several parametric variations are considered, three of which are reported here. They are: (i) the presence and absence of the ITP's 50 ft (15.24 m) infinite waveguide coil; (ii) closed (capped) and open terminations of the waveguide; and (iii) two different internal diameters of the waveguide.

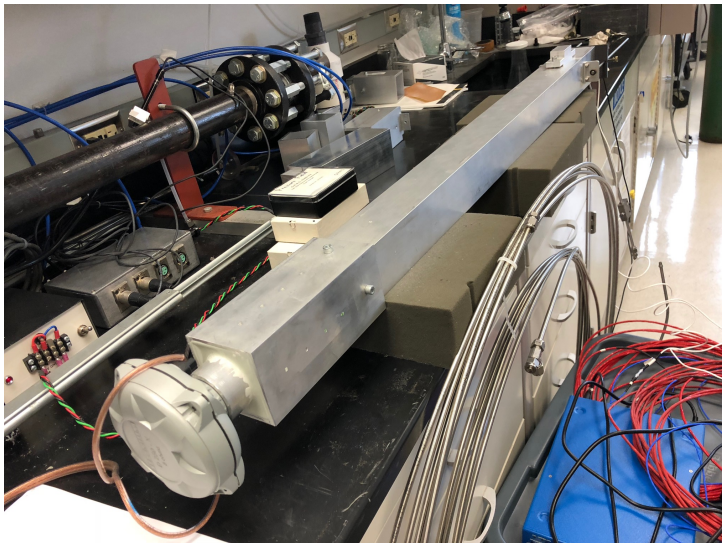

Fig. 1 Normal incidence tube with source driver (left) and termination plate (right) with ITP, flush-mounted microphone and pressure transducer

A particular ITP is shown in Fig. 3, without its infinite line connected. This ITP was used in the 2017 DART Core/Combustor-Noise Baseline Test [9]. The stainless steel tubing has a nominal inner diameter of 0.194 inch (4.93 mm) and the sense-line length is 14.5 inch (0.3683 m). The latter measurement has an uncertainty of about 2%. The Kulite® pressure sensor is flush mounted to the inner radius of the tube, using the block shown in the picture. A thermocouple is also mounted flush with the wall (i.e., not protruding into the tube) across from the pressure sensor. The assembly is shown uncapped (right) without the 50-ft coil attached. This configuration is referred to hereafter as the 2017 ITP.

Two other variable ITP configurations are also studied and will be referred to by their nominal outer diameter (OD) herein. The first, labeled the 1/4-inch-OD assembly, uses the same kind of stainless-steel tubing, a similar transducer tee (but does not allow for mounting of a thermocouple opposite the transducer), and same infinite coil as the 2017 ITP. The sense line is straight and can be selected to be 12, 24, or 48 inch (0.3048, 0.6096, or 1.2192 m) long. Figure 4 shows the 1/4-inch-OD ITP with the 12-inch sense line attached, but without the infinite line and pressure transducer connected. The second variable configuration, referred to here as the 1/8-inch-OD assembly, uses a waveguide made of stainless-steel tubing with a nominal OD of 1/8 inch. The nominal inner diameter is 0.055 inch (1.40 mm), however. Consequently, this represents a waveguide-diameter reduction by a factor of about 3.5 compared to the other two cases. The sense-line lengths for this case are also 12, 24, or 24 inch. The attachable infinite coil is also 50 ft long and is always capped at its end. Figure 5 shows the 1/8-inch-OD ITP connected to the infinite line, but without the sense line attached and pressure transducer installed.

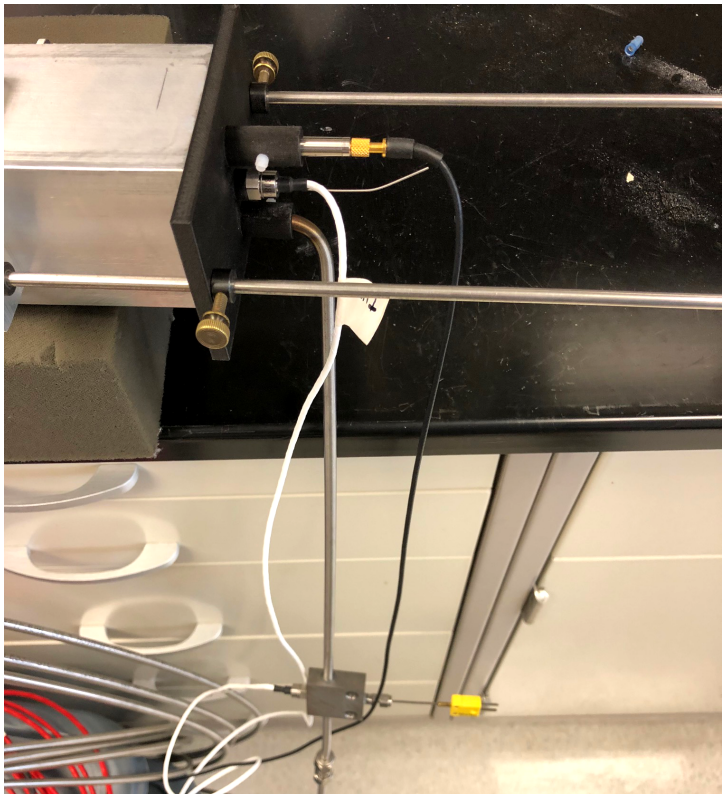

Fig. 2 Closeup view of the termination plate with ITP (bottom), flush-mounted microphone (top) and pressure transducer (center)

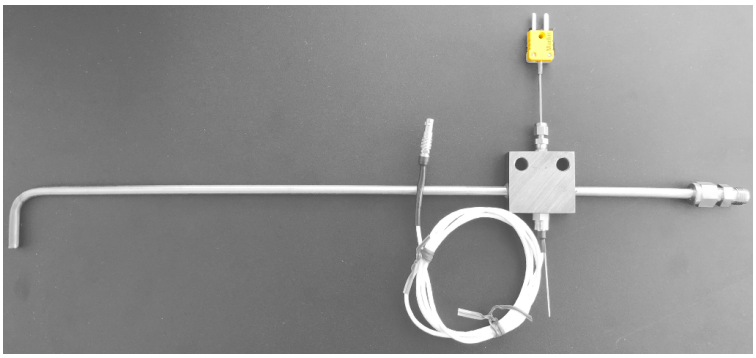

Fig. 3 ITP used in the 2017 DART Core/Combustor-Noise Baseline Test [9], with installed Kulite® (bottom with white cable) and thermocouple (top)

Fig. 4 1/4-inch-OD ITP with 12 inch sense line, but without installed Kulite® and coil

A National Instruments™ NI-1082 chassis with a PXIe-4499 analog-to-digital conversion (ADC) card is used for data acquisition. A Kulite® KSC-2 signal conditioner amplifies (but does not filter the Kulite® transducer signals). Data are collected at a rate of 200 kHz. The source driver uses a stimulus provided by a Stanford Research Systems function generator (DS360). The function generator produces a repeating 10 s logarithmic tone sweep from 500 Hz to 3 kHz

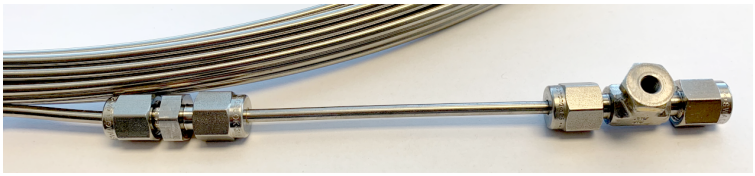

Fig. 5 1/8-inch-OD ITP connected to coil, but without 12 inch sense line and installed Kulite®

for a test duration of 240 s. For select test configurations, a sequence of single harmonics (roughly 1/3-octave-band center frequencies between 500 Hz and 3 kHz) are input, each with a 30 s sample duration, to verify the shape of the transfer function produced with the logarithmic sweep. The time series produced by the ADC are then post-processed using MATLAB scripts and routines. Cross- and auto-spectra are computed using the MATLAB function `cpsd` using a segment length of 16,384 points (12.2 Hz frequency resolution) for sweep cases and 32,768 points (6.1 Hz frequency resolution) for discrete-harmonic cases. The Hamming window and 50% segment overlap are used throughout.

The experimentally determined transfer function is then computed by dividing the cross-spectrum between the two signals of interest by the auto-spectrum of the signal that is considered as the reference,

$$H_{ij}(f) = G_{ij}(f)/G_{ii}(f), \tag{1}$$

where H_{ij}, G_{ij}, and G_{ii} denote the (one-sided) transfer function, cross- and auto-spectrum, respectively for the signals $s_i(t)$ and $s_j(t)$, with t designating time; s_i is the reference signal and f is the frequency. Note that both the transfer function and the cross-spectrum are complex quantities. In what follows, the microphone signal and the flush-mounted and ITP-Kulite® signals are designated as $s_1(t)$, $s_2(t)$, and $s_3(t)$, respectively. Excellent agreement was always found between sweep- and discrete-harmonic-determined transfer functions.

A. Typical Parameters During Testing

The atmospheric conditions in the room where the NIT is located were approximately standard atmospheric pressure and 20 °C (68 °F) temperature during the testing. Table 1 shows the relevant physical properties and parameters associated with the test. Using the values in Table 1, the shear-number parameter, see Eq. (A 3), for a given frequency

Table 1 Relevant Physical Properties and Parameters (SI)

ITP-line inner radius, 1/4 inch OD	r_o, m	2.4638×10^{-3}
1/8 inch OD	r_o, m	6.985×10^{-4}
mean temperature	T_o, K	293.15
mean pressure	p_o, kPa	101.325
mean density	ρ_o, kg/m^3	1.2041
gas constant	R, J/kg K	287.058
specific heat at constant pressure	c_p, J/kg K	1004.9
ratio of specific heats	γ	1.3999
adiabatic speed of sound	c_o, m/s	343.21
mean impedance	z_o, kg/m^{2}s	413.26
dynamic viscosity	μ, kg/ms	1.8361×10^{-5}
kinematic viscosity	ν, m^2/s	1.5249×10^{-5}
Prandtl number	σ	0.70858
shear number	W	$\sqrt{2\pi f r_o^2/\nu}$
frequency	f, Hz	500–3,000

can then be evaluated through

$$W = 1.5815\sqrt{f}, \tag{2a}$$

for the assemblies using waveguides with nominal OD of 1/4 inch and

$$W = 0.4484\sqrt{f} \tag{2b}$$

for nominal 1/8-inch OD cases. The square of the shear-number parameter represents the ratio of a diffusive time scale to the time scale of the oscillation. For the frequency range in the NIT test, this means that the shear parameter, falls in the range of about 35 to 87 for the 1/4-inch-OD cases and about 10 to 25 for the 1/8-inch-OD cases. The shear parameter W can, hence, be considered as large in the testing, i.e. the motion in the line is dominated by inertia effects. Since a value of W equal to ten can be considered as large, frequencies as low as 40 Hz would actually fall in the large-shear-number range for the 1/4-inch-OD assemblies.

III. Theory

A transfer, or frequency response, function is used to relate the unsteady pressure at the actual location of interest to the unsteady pressure measured at a remote location, using the ITP technique, when a direct measurement is not possible. The transfer function $H(f)$, where f is the frequency, provides magnitude and phase relationships between the desired and remote measurements. The magnitude change is given by $|H(f)|$ and the phase lag is given by $\phi = \arg[H(f)]$. The transfer function depends on the specific configuration details of the ITP. Iberall [12], Bergh and Tijdeman [13], and Samuelson [14] developed the theoretical framework for ITP transfer functions. For convenience,[a] the salient features and assumptions of basic ITP theory are summarized in Appendix A. The theoretical transfer function for the type of ITP configurations used here are worked out in Appendix B by following the recursive procedure introduced by Bergh [13].

The general result for the transfer function is given by Eq. (B 9). In this equation, $Q = 1$ if the line is capped, $Q = -1$ if the line is open, and $Q = 0$ if the line terminates into its own impedance (i.e., actually is infinite). V_T is the (effective) transducer volume. If the shear-number parameter, see Eq. (A 3), is large, this result can be further simplified. In this case, Eq. (B 9) reduces to Eq. (B 10). Even though this limit turns out to be valid for the frequency range of interest here, all computations are performed using Eq. (B 9) throughout this report.

A. Ideal Case

In what follows, the ideal case refers to the situation when the waveguide downstream of the transducer is infinitely long and the effective transducer volume is neglible, i.e. $Q = 0$ and $V_T = 0$. In this ideal case, Eq. (B 9) reduces to

$$H(f) = \mathrm{e}^{-\mathcal{H}L_S} = \mathrm{e}^{-\chi(f)L_S + \mathrm{i}\kappa(f)L_S}\,, \tag{3}$$

where $\mathcal{H}$, χ, and κ are defined by Eqs. (A 7b) and (A 9) and L_S is the sense-line length. Since the shear-number parameter turns out to be large for the cases of interest here, physical insights can be gleaned by using the approximate results in Eq. (A 20) instead. The leading-order magnitude and phase lag of the ideal transfer function are then given by

$$|H(f)| \approx \exp\left[-\frac{2\pi L_S f}{\sqrt{2}Wc_o}\left(1 + \frac{\gamma - 1}{\sqrt{\sigma}}\right)\right] = \exp\left[-\frac{L_S}{r_o}\sqrt{\pi\nu f/c_o^2}\left(1 + \frac{\gamma - 1}{\sqrt{\sigma}}\right)\right] \tag{4a}$$

and

$$\phi \equiv \arg\, H \approx \frac{2\pi L_S}{c_o} f\,, \tag{4b}$$

respectively. The exponential magnitude reduction depends linearly on the ratio of the sense-line length to the waveguide radius and the square root of the normalized frequency, or frequency paramter, $F = \omega\nu/c_o^2$. The leading-order phase lag simply reflects the well-known concept of signal flight-time delay. The most critical simplification used here, perhaps, is the assumption of a negligible effective transducer volume which otherwise would cause an impedance change within the tee.

B. Finite Waveguide

When the waveguide length, L_I, downstream of the transducer location is finite, the general transfer function, Eq. (B 9), will be dominated by resonance effects. To gain further insights for this case, it is instructive to neglect the

[a]These early references used what can today be considered somewhat outdated and cumbersome notation

transducer-volume effect, i.e. set $V_T = 0$ in Eq. (B 9). The transfer function then reduces to

$$H(f) = \frac{\mathrm{e}^{-\mathcal{H}L_S}\left(1 + Q\,\mathrm{e}^{-2\mathcal{H}L_I}\right)}{1 + Q\,\mathrm{e}^{-2\mathcal{H}(L_S+L_I)}}, \quad Q \neq 0, \tag{5}$$

where the complex quantity $\mathcal{H}(f)$ in general is given by Eq. (A 7b). Resonances occur when the denominator in Eq. (5) nearly vanishes.[b] Using the large-shear-number result, Eq. (A 20), it follows that the resonance frequencies approximately are given by

$$f_n \approx \frac{(n + \frac{1}{2})\,c_o}{2(L_S + L_I)}, \quad n = 0, 1, \ldots, \quad Q = 1, \tag{6a}$$

$$f_n \approx \frac{n\,c_o}{2(L_S + L_I)}, \quad n = 0, 1, \ldots, \quad Q = -1, \tag{6b}$$

for the terminated- and open-line cases, respectively.

C. Effective Transducer-Tee Volume

For a sufficiently long waveguide downstream of the transducer location, all waves reflected from its end point can be neglected at the transducer location. In this case, the transfer function, Eq. (B 9), simplifies to

$$H(f) = \mathrm{e}^{-\mathcal{H}L_S}\left[1 + \frac{\gamma V_T}{n_T 2\pi r_o^2 \mathcal{H}}\left(\frac{\omega}{c_o}\right)^2 \frac{J_0(\alpha)}{J_2(\alpha)}\left(1 - \mathrm{e}^{-2\mathcal{H}L_S}\right)\right]^{-1} \approx \mathrm{e}^{-\mathcal{H}L_S}\left[1 - \mathrm{i}\frac{\gamma V_T f}{n_T r_o^2 c_o}\left(1 - \mathrm{e}^{-2\mathcal{H}L_S}\right)\right]^{-1}, \tag{7}$$

where the last member represents the leading-order result in the large-shear-number limit. Eqs. (A 9) and (A 20), rather than Eq. (A 7b), should be used to evaluate $\mathcal{H}$ for the last member. Eq. (7) shows that the transfer-function magnitude, for a nonzero value of V_T, will exhibit undulations as the frequency is varied. As also pointed out in Appendix B, $V_T f/\pi r_o^2 c_o$ is the ratio of the transducer volume to the volume in the line corresponding to one acoustic wavelength of the perturbation motion and can be expected to be rather small for the cases studied in this report. However, it turns out that it must be accounted for in the analysis.

Determining the effective transducer volume turns out to be a cumbersome task. First, the volume under the screen, say V_C, of a typical Kulite® pressure transducer can be estimated by using Eg. 7 of Hurst et al. [15] and the information contained in their Figs. 10 and 11 for a XTE-190 transducer with standard B screen. It is believed that the geometrical layout is sufficiently similar, if not identical, to the transducer used in the current work. This leads to the estimate of $V_C = 3.50 \times 10^{-8}\,\mathrm{m}^3$ for the intrinsic transducer cavity volume. Second, the transducer is flush mounted to the inner radius of the line. This means that there is an additional tee volume that needs to be accounted for. Furthermore, if there is a thermocouple, its additional mounting volume needs to be included.

For the assemblies using the nominal 1/4-inch-OD lines, the additional mounting volume $V_M = 4.2 \times 10^{-9}\,\mathrm{m}^3$ for the thermocouple design and $V_M = 2.6 \times 10^{-9}\,\mathrm{m}^3$ otherwise. Adding up the transducer-cavity and mounting volumes gives the estimates $V_T = 3.92 \times 10^{-8}\,\mathrm{m}^3$ and $V_T = 3.76 \times 10^{-8}\,\mathrm{m}^3$ for the two 1/4-inch-OD cases with and without a thermocouple tee design, respectively. However, it turns out that these estimates of the effective transducer volume are too small to explain the observed undulations (see below) in the transfer-function magnitude. A modified approach is therefore needed. It is quite conceivable that the line volume under the transducer tap, $2\pi r_o^3$, should be included in the effective transducer volume.

For the nominal 1/4-inch-OD waveguides, the line volume under the tap is $0.9397 \times 10^{-7}\,\mathrm{m}^3$ and, consequently, V_T would typically be around $1.32 \times 10^{-7}\,\mathrm{m}^3$ when this volume is included. The procedure settled on is to start with this estimated value for V_T and then adjust it until a reasonable agreement between theory and experiment is acheived in a certain frequency range, say 500–1,000 Hz. No optimization procedure is used here, but could certainly be employed for this purpose. An upwards adjustment of V_T can be justified by the fact that the value of the polytropic expansion coefficient $1 \leq n_T \leq \gamma$ is not known. It is found that that the effective transducer volume $V_T = 1.5 \times 10^{-7}\,\mathrm{m}^3$ leads to reasonable agreements. This value falls within the expected adjustment range of up to plus 40 percent. The theoretical predictions presented in this report for the cases with nominal 1/4-inch-OD waveguides all use this value.

For the 1/8-inch-OD assemblies, line volume under the tap is $0.2141 \times 10^{-8}\,\mathrm{m}^3$ and the sum of this volume and the intrinsic transducer volume is $3.71 \times 10^{-8}\,\mathrm{m}^3$. However, it is found that the larger than expected value of $V_T = 9.0 \times 10^{-8}\,\mathrm{m}^3$ is needed to achieve reasonable agreements in this case.[c]

[b] The denominator in Eq. (5) only vanishes to leading order in the large-W limit.

[c] There is a funnel-shaped volume between the transducer face and the line yet to be accounted for however.

IV. Results

Auto-spectra and transfer functions are presented for select ITP configurations, including cases with and without a 50-ft infinite coil attached as well as with differing sense-line lengths. For cases with the nominal 1/4-inch-OD coil attached, the coil termination did not affect the results—indicating that the coil length can be considered as effectively infinite—and only capped coil results are presented here. Based on the experience with the nominal 1/4-inch-OD coil, only a capped termination is used for the nominal 1/8-inch-OD coil.

The first set of cases to be presented are results obtained using the 2017 ITP in three configurations, namely, uncapped without the coil, capped without the coil, and with a capped coil. Figure 6 shows the (12.2 Hz binwidth) auto-spectra,

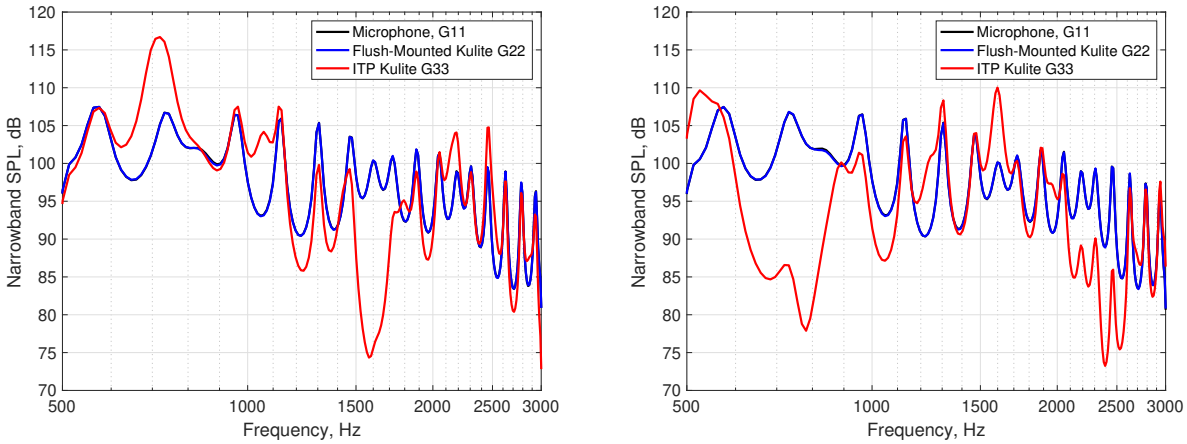

Fig. 6 Narrowband (12.2 Hz) SPL levels measured by the three sensors for the 2017 ITP without a coil: (a) open termination; (b) capped termination

in terms of the narrowband sound-pressure level (SPL), for the three sensors. That is, it shows $10 \times \log_{10}(G_{ii}/P_{ref}^2)$ for $i = 1, 2, 3$, with $P_{ref} = 2 \times 10^{-5}$ Pa. In both panels, the ITP is not connected to the infinite coil. Panel (a) and (b) are for ITP configurations with an open and a capped termination of the short line downstream of the sensor location, respectively. The black curves denote the microphone SPL and, on the scale used here, are masked by the blue curves that represent the flush-mounted-Kulite® SPL. The red curves show the ITP-Kulite® SPL. As fully expected, both panels clearly show the effects of reflections and resonances caused by the finite line length after the ITP-transducer tee. The contrast in the ITP-Kulite® response between the two panels is caused by the different end conditions. The undulation in the blue (and black) curves is caused by standing wave resonances inside the NIT. If the NIT had been infinitely long, then the logarithmic-sweep would have led to a pink-noise-like spectrum (even though being fully deterministic). Furthermore, the microphone signal generally will be used as the reference signal in what follows since the NIT-interior measurements track exceptionally well in both cases shown here.

Figures 7 and 8 show the experimental and theoretical transfer functions between the NIT microphone and the ITP transducer for the configurations analyzed in Fig. 6, i.e., the 2017 ITP without the infinite coil attached with open and capped terminations, respectively. In these figures, panels (a) and (b) show the transfer-function magnitude and phase lag, respectively. The red curves are the experimentally determined results. The dot-dash blue curves are the theoretical predictions using Eq. (B 9), with an effective transducer-tee volume of $V_T = 1.5 \times 10^{-7}$ m^3. The transfer function is actually dominated in these cases by the finite-length effects of the assembly and the assumed value of V_T has a negligible effect on the results here. The dashed black lines are the theoretical results for the ideal situation, i.e., when the line after the transducer tee is infinitely (or sufficiently) long and the effective transducer volume V_T is neglected. The theoretical results track the experimental ones very well, with the exception of detectable magnitude errors at resonant frequencies. However, these two configurations are, in some sense, extreme and would not be used in practice. They are included in the present study only as a test of the theoretical-prediction capability of Eq. (B 9).

The second set of results is comprised of measurements obtained using several variable-sense-line-length, 1/4-inch-OD waveguide, configurations. Figure 9 shows the (12.2 Hz binwidth) narrowband sound-pressure level (SPL), for the three sensors. In both panels, the ITP has a capped termination. Panel (a) and (b) are for ITP configurations without and with the infinite coil attached, respectively. The microphone SPL (solid black) curves are again masked by the flush-mounted-Kulite® SPL (solid blue) curves. The ITP-Kulite® SPL for a 12-inch sense line is shown using red lines

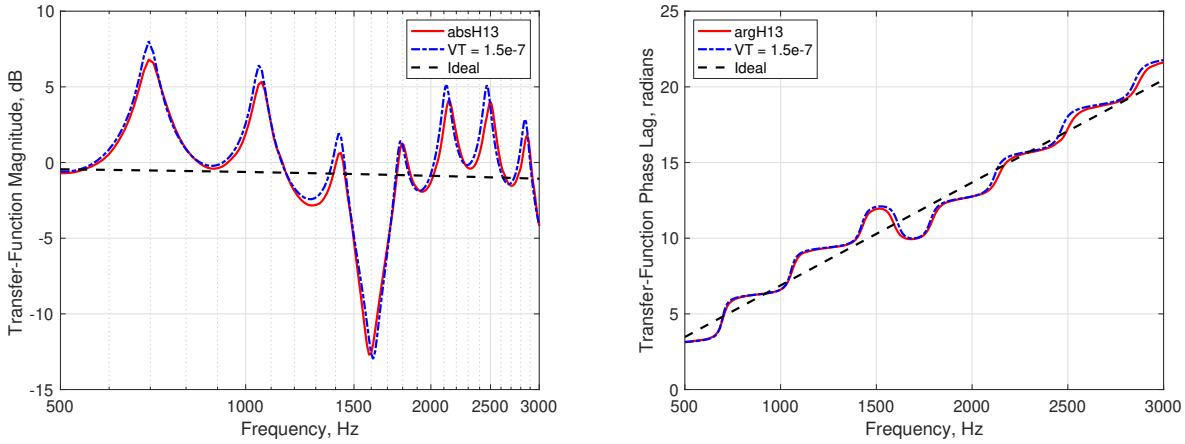

Fig. 7 Experimental and theoretical transfer functions for the uncapped 2017 ITP without coil: (a) magnitude and (b) phase lag

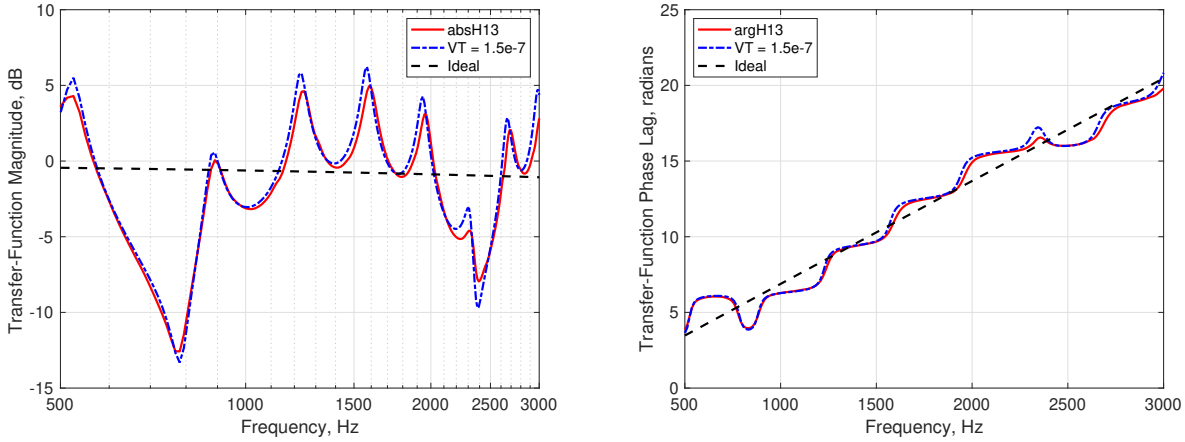

Fig. 8 Experimental and theoretical transfer functions for the capped 2017 ITP without coil: (a) magnitude and (b) phase lag

in both panels. For 24-inch and 48-inch sense lines, the ITP-Kulite® SPL levels are shown using magenta and rusty-red lines, respectively, in the right panel. The sense-line length is also indicated in the legends by the numbers 12, 24, and 48. As before, panel (a) clearly shows the effects of reflections and resonances caused by the finite line length after the ITP-transducer tee. Panel (b) shows that, with the infinite-line coil attached, the ITP-Kulite® SPL clearly tracks the SPL inside the NIT, but with an attenuation that increases as the frequency gets larger as well as with increasing sense-line length.

Figure 10 shows the experimental and theoretical transfer functions between the NIT microphone and the ITP transducer for the configuration analyzed in Fig. 9(a), i.e., the nominal 1/4-inch-OD ITP assembly with a 12-inch sense line and a capped termination, but without the infinite coil attached. Panels (a) and (b) show the transfer-function magnitude and phase lag, respectively. The red curves are the experimentally determined results. The dot-dashed blue lines are the predictions based on Eq. (B 9), with $V_T = 1.5 \times 10^{-7}$ m^3. The dashed black lines are the idealized theoretical results, i.e., when the line after the transducer tee has a perfectly matched termination (i.e. the line is infinitely long) and the effective transducer volume is zero. Again, the theoretical results agree very well with the experimental ones, except for some magnitude deviations at resonance frequencies.

Figure 11 shows the experimental and theoretical transfer functions between the NIT microphone and the ITP transducer for the configuration analyzed in Fig. 9(b), i.e., the nominal 1/4-inch-OD ITP assembly with a capped infinite

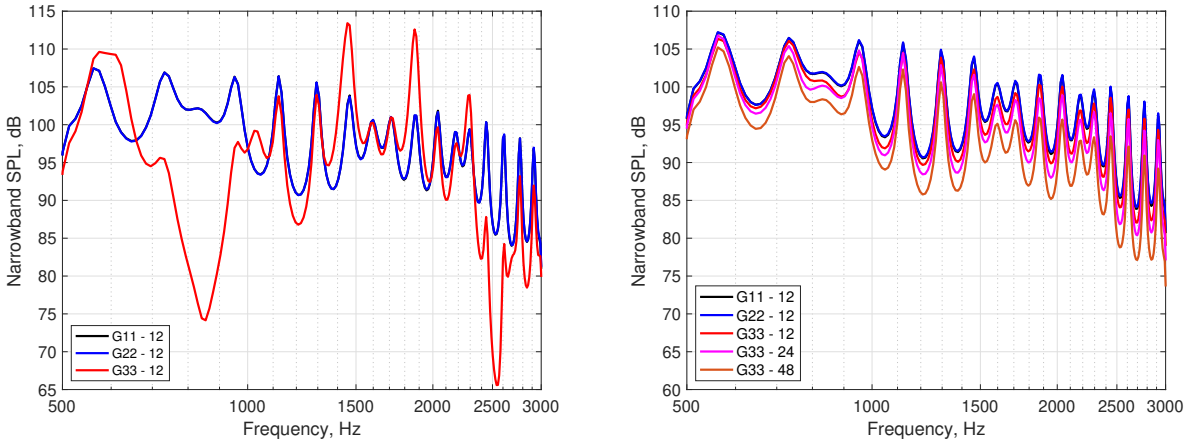

Fig. 9 Narrowband (12.2 Hz) SPL levels measured by the three sensors for the nominal 1/4-inch-OD ITP assembly: (a) capped, without coil—12-inch sense line; (b) capped, with coil—12-, 24-, and 48-inch sense line

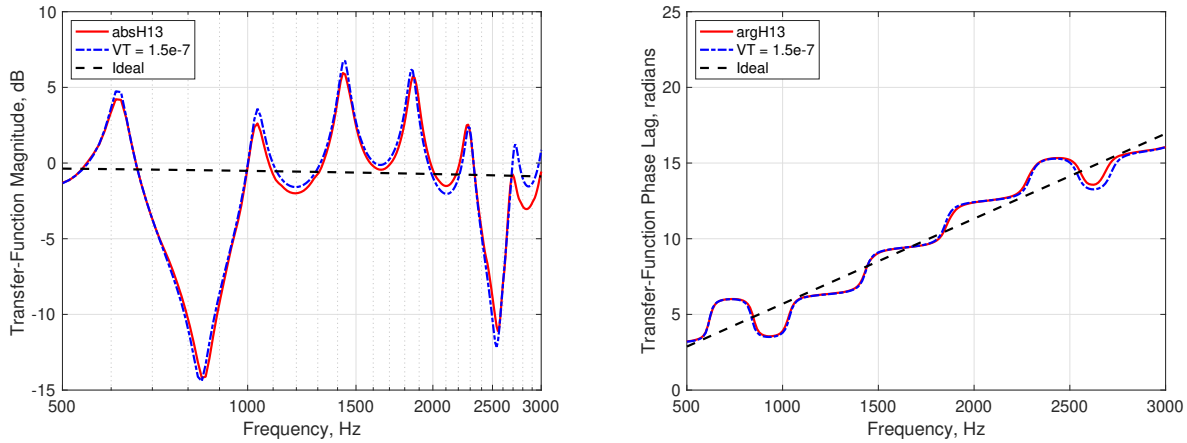

Fig. 10 Experimental and theoretical transfer functions for the capped ITP without coil: (a) magnitude and (b) phase lag

coil attached for various values of the sense-line length. Panels (a) and (b) show the transfer-function magnitude and phase lag, respectively. The red, magenta, and rusty-red curves are the experimentally determined results for 12-, 24-, and 48-inch sense-line lengths, respectively. The dot-dashed blue, cyan, and blue-gray lines are the theoretical results, Eq. (B 9), with $V_T = 1.5 \times 10^{-7}$ m^3 for the sense-line lengths of 12, 24, and 48 inch, respectively. The dashed black lines depict the ideal theoretical transfer-function behavior. The theoretical and experimental transfer-function-magnitude results compare very well for frequencies up to about 1 kHz. Thereafter, the agreement increasingly deteriorates as the frequency increases. This deviation is decreasing with increasing sense-line length however. The largest magnitude deviation, observable in this figure, is estimated to be less than about 1 dB, which is rather close to reasonable assumptions about measurement uncertainties in real-engine tests. The measured transfer-function phase lag is well predicted by simply applying the leading-order time-of-flight correction.

The third set of measurements contains results for several variable-sense-line-length, 1/8-inch-OD waveguide configurations. The ITP has the capped infinite coil attached in all assemblies. Figure 12 shows the (12.2 Hz binwidth) narrowband sound-pressure level (SPL) for the three sensors. The microphone SPL (solid black) curve is, as above, masked by the flush-mounted-Kulite® SPL (solid blue) curve. The ITP-Kulite® SPL levels for 12-, 24-, and 48-inch sense-line lengths are shown using red, magenta, and rusty-red lines, respectively. The ITP-Kulite® SPL levels clearly track the SPL inside the NIT, but with an attenuation that increases as the frequency gets larger as well as with increasing

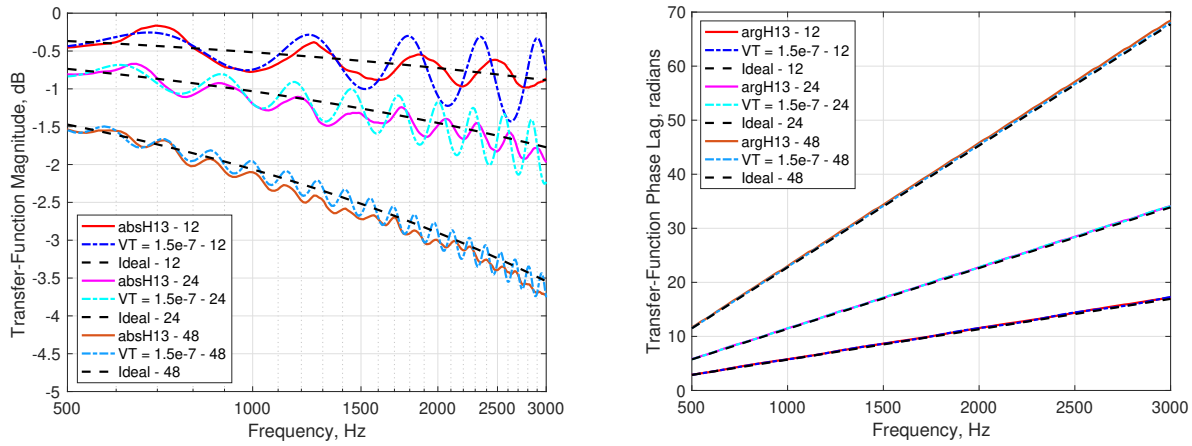

Fig. 11 Experimental and theoretical transfer functions for the nominal 1/4-inch-OD ITP assembly with a capped coil: (a) magnitude and (b) phase lag

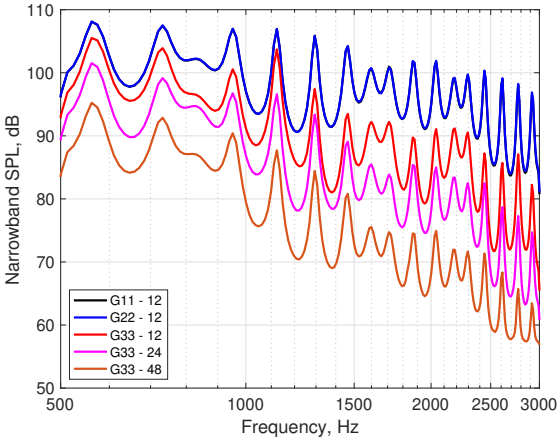

Fig. 12 Narrowband (12.2 Hz) *SPL* levels measured by the three sensors for the nominal 1/8-inch-OD ITP assembly with a capped coil and 12-, 24-, or 48-inch sense line

sense-line length. Both effects are more pronounced, as can be expected, compared to the corresponding 1/4-inch-OD cases.

Figure 13 shows the experimental and theoretical transfer functions between the NIT microphone and the ITP transducer corresponding to the configurations in Fig. 12, i.e., the 1/8-inch-OD ITP with a capped infinite coil attached and various sense-line lengths. Panels (a) and (b) show the transfer-function magnitude and phase lag, respectively. The red curves are the experimentally determined results for a 12-inch sense-line length; the magenta curves are the experimentally determined results for a 24-inch sense-line length; and the rusty-red curves are the experimentally determined results for the 48-inch sense-line length. The dot-dashed blue, cyan, and blue-gray lines are the theoretical results, Eq. (B 9), with $V_T = 9.0 \times 10^{-8}\,\mathrm{m}^3$ for the corresponding sense-line lengths. The dashed black lines show the ideal transfer-function behavior. The theoretical and experimental transfer-function-magnitude results compare well for frequencies up to about 1 kHz. Thereafter, the agreement deteriorates—although there is a frequency range, approximately 2.2–2.6 kHz, with again a reasonable agreement. The reason for later the region is not fully clear, but the more complex undulations observed for these assemblies are most likely caused by a resonance due to an unintended impedance change somewhere in the system. In contrast to the 1/4-inch-OD cases, the agreement in the 500-1,000 Hz frequency region is actually better for shorter sense lines. However, this could be another manifestation due to the suspected unintended impedance change. The measured transfer-function phase lag is still relatively well predicted by

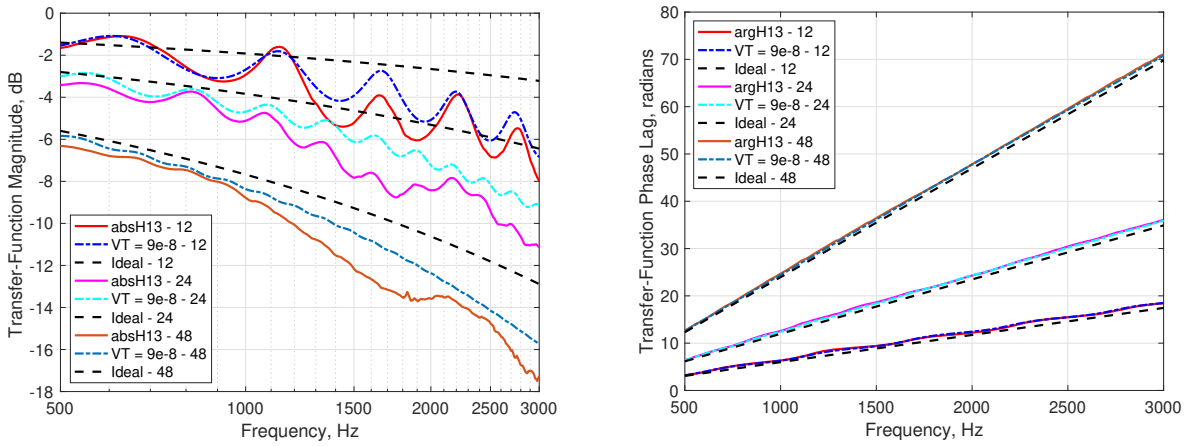

Fig. 13 Experimental and theoretical transfer functions for the nominal 1/8-inch-OD ITP assembly with a capped coil: (a) magnitude and (b) phase lag

simply applying the leading-order time-of-flight correction. However, the influence of the effective transducer volume on the phase lag is more pronounced than in the previous set.

The undulations in both transfer-function magnitude and phase lag are the result of a standing wave pattern within the ITP sense line due to reflections caused by impedance changes within the transducer tee. Using the determined effective transducer volumes, it follows that at, say 1 kHz, the ratios of the transducer volume to the volume in the line corresponding to one acoustic wavelength, $V_T\ f/\pi r_o^2 c_o$, are 0.023 and 0.171 in the 1/4-inch-OD and 1/8-inch-OD cases, respectively. Both values are small, but the latter is about one-order of magnitude larger than the former. Consequently, the effects of the effective transducer volume should be stronger for the assembly with the smaller inner diameter, which explains the reason behind some of the observed different behaviors.

V. Conclusions

The use of unsteady pressure transducers in an ITP arrangement allows measurements in the hostile environment found for example in the core of gas-turbine engines, i.e., where the transducers themselves would not survive. In order to extract accurate magnitude and phase information at the desired measurement location, a transfer function, that relates the desired and actual measurements for the actual instrumentation layout, needs to be established and validated.

A transfer function was constructed using established procedures [13] and compared to select experimental results obtained using a slightly modified NIT at NASA GRC. In general, the theoretical predictions compare very well with the experimental data up to about 1 kHz, which covers the most relevant frequency range for turbofan core/combustor noise. Consequently, the theoretical transfer function can be used to correct the measured unsteady-pressure data for the ITPs studied here if the interest is limited to that frequency range. If higher frequencies are of interest, then it is necessary to apply the slightly less efficient procedure of correcting the data using the measured transfer function.

The study also showed that the transducer/tee-volume effect plays a cruical role in the ITP physics leading to undulations in the transfer-function magnitude and phase lag. These undulations become more pronounced as the frequency is increased and as the waveguide (inner) diameter is reduced. Even though the transducer/tee-volume term in the theoretical transfer function, at first glance, might appear not to be too significant, it needs to be included in predictions. As is well known in many fields, even very small terms can have an observable impact at or near resonance conditions as indeed is borne out here.

Additional conclusions to be drawn, or lessons to be learned, from the current work are: First, as large a diameter of the ITP line as practical (matched to the transducer size) should be used. Not because this would lead to less attenuation than for a thinner line, but because this would minimize the effects of the finite effective-transducer volume as well as unintended imperfections in the implementation of the ITP design. Second, it is important to test, to the fullest extent possible, each ITP for subtle imperfections, before installation in an engine or rig. Third, a good tee design is imperative, particularly if higher frequencies are of interest.

Appendices

A. Brief Summary of ITP Theory

This appendix gives a very brief summary of the basic concepts of infinite-tube-probe (ITP) acoustics. The main references are the papers by Iberall [12], Bergh and Tijdeman [13], and Samuelson [14]. The major assumptions for the theory are that the flow in the instrumentation tube is laminar and that the interior radius of the tube is small compared to both the length of the sense line and the acoustic wavelengths. Furthermore, as in [12–14], there is no purge flow in the ITP and only axisymmetric perturbations are considered.

1. General Solution

The unsteady fluctuations are assumed to be small enough such that they can be described by linearized versions of the equations of continuity, momentum, energy, and state. In addition, since the diameter of the tube is very small compared to any characteristic streamwise length scale, it turns out that the radial velocity component will be small compared to the streamwise velocity component. It then also follows that the pressure fluctuation will depend only on the streamwise coordinate x and time t, whereas the other unsteady quantities also depend on the radial coordinate r. Consequently, using the usual normal-mode assumption for the perturbations, the dependent variables can be expressed as

$$\rho = \rho_o + \text{Real}\left[\hat{\rho}(x,r)\mathrm{e}^{-\mathrm{i}\omega t}\right], \tag{A 1a}$$

$$p = p_o + \text{Real}\left[\hat{p}(x)\mathrm{e}^{-\mathrm{i}\omega t}\right], \tag{A 1b}$$

$$T = T_o + \text{Real}\left[\hat{\theta}(x,r)\mathrm{e}^{-\mathrm{i}\omega t}\right], \tag{A 1c}$$

$$\boldsymbol{u} = \text{Real}\left[\hat{u}(x,r)\mathrm{e}^{-\mathrm{i}\omega t}\right]\hat{\mathrm{i}} + \text{Real}\left[\hat{\mathrm{v}}(x,r)\mathrm{e}^{-\mathrm{i}\omega t}\right]\hat{\mathrm{r}}, \tag{A 1d}$$

$$e = e_o + c_v(T_o)\,\text{Real}\left[\hat{\theta}(x,r)\mathrm{e}^{-\mathrm{i}\omega t}\right], \tag{A 1e}$$

where ρ, p, T, $\boldsymbol{u}$, and e denote density, pressure, temperature, velocity vector, and specific internal energy, respectively; $\hat{\mathrm{i}}$ and $\hat{\mathrm{r}}$ are the unit vectors in the streamwise and radial directions; $c_v(T_o)$ is the specific heat at constant volume evaluated at temperature T_o; $\omega = 2\pi f$ is the angular frequency of the perturbation motion and f is the frequency. The mean-flow variables, denoted by the subscript 'o', are all constants.

It follows that the solution to the normal-mode form of the streamwise momentum equation, that is finite at the origin and satisfies the no-slip condition on the tube wall, is given by

$$\hat{u}(x,r) = -\frac{\mathrm{i}}{\omega\rho_o}\frac{\mathrm{d}\hat{p}(x)}{\mathrm{d}x}\left[1 - \frac{J_0(\alpha r/r_o)}{J_0(\alpha)}\right], \tag{A 2}$$

where J_m is the Bessel function of the first kind of order m, r_o is the tube radius, $\alpha = \mathrm{e}^{\mathrm{i}\pi/4}W$ has been introduced for notational convenience, and

$$W = \sqrt{\omega\rho_o r_o^2/\mu} \tag{A 3}$$

is a nondimensional parameter known as the shear number.[d] Its square represents the ratio of the inertia terms to the viscous terms in the streamwise momentum balance. Put in another way, its square represents the ratio of the diffusive time scale, $\rho_o r_o^2/\mu$, to the time scale of the oscillation, $1/\omega$.

Multiplying Eq. (A 2) by the mean density ρ_o and integrating the result across the tube cross-sectional area produces

$$\hat{\dot{m}}(x) = \frac{\mathrm{i}\pi r_o^2}{\omega}\frac{J_2(\alpha)}{J_0(\alpha)}\frac{\mathrm{d}\hat{p}}{\mathrm{d}x}, \tag{A 4}$$

where $\dot{m} = \text{Real}\left[\hat{\dot{m}}\exp(-\mathrm{i}\omega t)\right]$ is the unsteady mass-flow rate.

Under the customary assumption that the heat capacity of the rigid wall is sufficiently large so that the temperature fluctuations will be zero at the wall, it follows that the solution to the normal-mode form of the energy equation reads

$$\hat{\theta}(x,r) = \frac{\hat{p}(x)}{\rho_o c_p}\left[1 - \frac{J_0(\alpha' r/r_o)}{J_0(\alpha')}\right], \tag{A 5}$$

[d] In contrast to, say Ref. 13, nondimensional parameters are strictly taken as real numbers here.

where $\alpha' = \alpha\sqrt{\sigma}$, with $\sigma = \mu c_p/\lambda$ being the Prandtl number; c_p is the specific heat at constant pressure, μ is the dynamic viscosity, and λ is the heat conductivity (all evaluated at T_o). The normal-mode form of the linearized equation of state, i.e, the linearized ideal-gas law, then shows that the density perturbation is given by

$$\hat{\rho}(x,r) = \frac{\hat{p}(x)}{c_o^2}\left[1 + (\gamma-1)\frac{J_0(\alpha' r/r_o)}{J_0(\alpha')}\right], \tag{A 6}$$

where $c_o = \sqrt{\gamma R T_o}$ is the adiabatic speed of sound, $\gamma = c_p/c_v$ is the ratio of specific heats and R is the gas constant.

Substituting Eqs. (A 2) and (A 6) into the normal-mode form of the continuity equation, integrating the resulting equation with respect to the radial coordinate, and applying the condition that the normal velocity must vanish at the outer wall shows that the normal-mode pressure must satisfy

$$\frac{\mathrm{d}^2\hat{p}}{\mathrm{d}x^2} - \mathcal{H}^2\hat{p} = 0, \tag{A 7a}$$

where

$$\mathcal{H}^2 = \left(\frac{\omega}{c_o}\right)^2 \frac{J_0(\alpha)}{J_2(\alpha)}\left[\gamma + (\gamma-1)\frac{J_2(\alpha')}{J_0(\alpha')}\right], \tag{A 7b}$$

in order for the radial velocity perturbation to vanish at center axis of the tube. The implicit branch cut in Eq. (A 7b) is taken along the negative real axis such that the real part of the complex parameter $\mathcal{H}$ is positive. Keeping causality in mind, it follows that the general solution to Eq. (A 7) is

$$\hat{p}(x) = A^+ \mathrm{e}^{-\mathcal{H}x} + A^- \mathrm{e}^{\mathcal{H}x} = A^+ \mathrm{e}^{-\chi x + \mathrm{i}\kappa x} + A^- \mathrm{e}^{\chi x - \mathrm{i}\kappa x}, \tag{A 8}$$

where A^+ and A^- are arbitrary constants (to be determined by streamwise boundary conditions) and

$$\mathcal{H} = \chi - \mathrm{i}\kappa, \tag{A 9}$$

where χ, the streamwise decay rate, and κ, the streamwise wave number, have been introduced. It is clear that the first term in Eq. (A 8) represents a pressure disturbance that entered at an upstream location and is decaying in the downstream location. The other term represents a reflected perturbation decaying in the upstream direction.

2. Transducer Model

The placement of a pressure transducer (or transducer tap) at a location, say $x = x_T$, in the tube will lead to an impedance discontinuity. Consequently, there will be a reflected wave generated at that location. The conditions to be applied at $x = x_T$ are: (i) the fluctuating pressures upstream of, downstream of, and inside the transducer are the same; and (ii) the unsteady mass-flow rate into the transducer equals the difference between the corresponding upstream and downstream values. Furthermore, it is assumed here that there is no area change of the line at the transducer location.

It is usually assumed that the properties inside a transducer only depend on time. It is also assumed that the compression process of the gas inside the transducer is polytropic, i.e. some heat exchange can take place with the surroundings. In this case, the equation of state reads

$$p_T \rho_T^{-n_T} = \text{constant}, \quad 1 \le n_T \le \gamma, \tag{A 10}$$

where p_T and ρ_T denote the pressure and density in the transducer. If $n_T = 1$ then the process is isothermal, i.e., sufficient heat exchange takes place for it to remain at constant temperature. If $n_T = \gamma$, then the process is adiabatic.

By making the normal-mode assumption, i.e., $\rho_T = \rho_o + \text{Real}\left[\hat{\rho}_T \mathrm{e}^{-\mathrm{i}\omega t}\right]$ and $p_T = p_o + \text{Real}\left[\hat{p}_T \mathrm{e}^{-\mathrm{i}\omega t}\right]$, it follows that the mass-flow rate into the transducer is given by

$$\hat{\dot{m}}_T = -\mathrm{i}\frac{\gamma\omega}{n_T c_o^2} V_T \hat{p}(x_T), \tag{A 11}$$

where V_T is the transducer volume and $\hat{p}(x_T)$ is the pressure normal-mode amplitude in the line at the transducer location x_T. Finally, conservation of mass then yields the transducer model

$$\left[\frac{\mathrm{d}\hat{p}}{\mathrm{d}x}\right]_{x_T-}^{x_T+} = \frac{\gamma V_T}{n_T \pi r_o^2}\left(\frac{\omega}{c_o}\right)^2 \frac{J_0(\alpha)}{J_2(\alpha)}\hat{p}(x_T). \tag{A 12}$$

The pressure is continuous across the transducer location, but there is a discontinuity in its slope given by Eq. (A 12).

3. Small- and Large-Shear-Number Limits

Let's first consider the limit of small shear numbers, i.e., it is assumed that $W << 1$. Since the Prandtl number is of order unity, both $|\alpha|$ and $|\alpha'|$ are then very small. For small values of its argument the Bessel function of the first kind behaves as $J_m(z) \approx (\frac{1}{2}z)^m/m!$ [16]. It follows that

$$\mathcal{H} \approx (1-\mathrm{i})\frac{2\omega\sqrt{\gamma}}{c_o W} \tag{A 13}$$

and that

$$\hat{u}(x,r) \approx -\frac{1}{4\mu}\frac{\mathrm{d}\hat{p}}{\mathrm{d}x}(r_o^2 - r^2)\,. \tag{A 14}$$

the latter is simply a Poiseuille flow driven by the local (and instantaneous) pressure gradient. That is when the oscillation is slow enough, the diffusive forces have enough time to penetrate the whole flow field. The unsteady mass-flow rate is given by

$$\hat{\dot{m}} \approx -\frac{\rho_o \pi r_o^4}{8\mu}\frac{\mathrm{d}\hat{p}}{\mathrm{d}x}\,, \tag{A 15}$$

which can be obtained by taking the small-W limit of Eq. (A 4) or simply by integrating Eq. (A 14) across the tube area.

Second, let's consider the opposite limit, i.e. the case when $W >> 1$. This is the limit that is of actual practical importance for the situation considered in this report. Both $|\alpha|$ and $|\alpha'|$ are then very large. Formula 9.2.5 (and supporting formulas) in Abramowitz and Stegun [16] shows that the Bessel function of the first kind for large values of its argument behaves as

$$J_m(z) \approx \sqrt{\frac{2}{\pi z}}\left[\cos(z - \frac{m\pi}{2} - \frac{\pi}{4}) - \frac{4m^2-1}{8z}\sin(z - \frac{m\pi}{2} - \frac{\pi}{4})\right], \quad |\arg z| < \pi\,. \tag{A 16}$$

Since $\arg\alpha = \arg\alpha' = \pi/4$, It follows that

$$J_m(\alpha) \approx \sqrt{\frac{1}{2\pi\alpha}}\left(1 - \mathrm{i}\frac{4m^2-1}{8\alpha}\right)\exp\left[-\mathrm{i}\left(\alpha - \frac{m\pi}{2} - \frac{\pi}{4}\right)\right], \tag{A 17}$$

with an identical formula involving α'. Hence, it follows that

$$J_2(\alpha)/J_0(\alpha) \approx -\left(1 - \frac{2\mathrm{i}}{\alpha}\right) \quad \text{as} \quad W \to \infty, \tag{A 18}$$

with an analogous formula when the argument is α'. Hence, for $W >> 1$,

$$\mathcal{H} \approx -\mathrm{i}\left(\frac{\omega}{c_o}\right)\left[1 + \frac{\mathrm{i}}{\alpha}\left(1 + \frac{\gamma-1}{\sqrt{\sigma}}\right)\right], \tag{A 19}$$

where the sign has been picked such that the real part is positive. Thus,

$$\chi \approx \frac{\omega}{\sqrt{2}Wc_o}\left(1 + \frac{\gamma-1}{\sqrt{\sigma}}\right), \tag{A 20a}$$

$$\kappa \approx \frac{\omega}{c_o}\left[1 + \frac{1}{\sqrt{2}W}\left(1 + \frac{\gamma-1}{\sqrt{\sigma}}\right)\right] \approx \frac{\omega}{c_o}\,. \tag{A 20b}$$

Since the shear number W, is proportional to the square root of the angular frequency, Eq. (A 20a) shows that the streamwise decay rate, χ, increases as the square root of the perturbation frequency. The perturbation essentially propagates with its free-field wave number. If the first-order correction thereof is included, Eq. (A 20b) shows that there is a small amount of dispersion, which probably can be ignored in many situations.

It also follows that

$$\hat{u}(x,r) \approx -\frac{\mathrm{i}}{\rho_o\omega}\frac{\mathrm{d}\hat{p}(x)}{\mathrm{d}x}\left[1 - \exp(-\mathrm{e}^{-\mathrm{i}\frac{\pi}{4}}\eta)\right], \tag{A 21a}$$

where

$$\eta = W(r_o - r)/r_o \tag{A 21b}$$

is a boundary-layer coordinate measured from the outer boundary and increasing towards the interior of the flow region. Thus, in this limit, the incident and reflected perturbations propagate with the adiabatic speed of sound as unsteady plug flows that are adjusted to zero at the solid wall through a thin boundary layer. The unsteady mass-flow rate is given by

$$\hat{m} \approx -\frac{\mathrm{i}\pi r_o^2}{\omega}\frac{\mathrm{d}\hat{p}(x)}{\mathrm{d}x} + O(1/W), \tag{A 22}$$

which is either obtained by a large-W expansion of (A 4) or by directly integrating Eq. (A 21a) across the tube area.

B. Two-Segment-Probe Analysis

A two-segment line will be analyzed here using the recursive approach developed by Bergh and Tijdeman.[13] The line has two equal-area segments of lengths $L_1 = L_S$ and $L_2 = L_I$, respectively. In general, the infinite line is much longer than the sense line, i.e., $L_I >> L_S$. The pressure transducer (or transducer tap) is located at the junction of these segments, i.e., at $x = x_T = L_S$.

The solution (A 8) in the two segments can be written as

$$\hat{p}^{(j)}(x_j) = A_j^+ \mathrm{e}^{-\mathcal{H}x_j} + A_j^- \mathrm{e}^{\mathcal{H}x_j}, \quad j = 1, 2, \tag{B 1}$$

where $x_1 = x$ and $x_2 = x - L_S$. Evaluating Eq. (B 1) at the entrance and exit of a segment, and then solving the resulting equations, shows that, for $j = 1, 2$,

$$A_j^+ = \frac{\hat{p}_{j-1}\mathrm{e}^{\mathcal{H}L_j} - \hat{p}_j}{2\sinh(\mathcal{H}L_j)}, \tag{B 2a}$$

$$A_j^- = \frac{\hat{p}_j - \hat{p}_{j-1}\mathrm{e}^{-\mathcal{H}L_j}}{2\sinh(\mathcal{H}L_j)}, \tag{B 2b}$$

where $\hat{p}_j$ denotes the value of the pressure at the segment exit and $\hat{p}_{j-1}$ is the exit pressure of the previous segment, i.e., the inlet pressure of the current segment.

1. Second Segment

The second segment is the infinite-line part of the ITP. There are three boundary conditions at its exit that need to be considered. First, the line can be capped at the end. Then the streamwise velocity must vanish at the end location, which means that $\mathrm{d}\hat{p}/\mathrm{d}x = 0$ for $x_2 = L_I$. Second, the line could be open at the end. In this case there is a pressure node at the exit, i.e., $\hat{p} = 0$ for $x_2 = L_I$. Finally, the line could be terminated into its own impedance, which means that it is actually infinite. These three situations can be described in terms of a reflection coefficient Q, by letting

$$A_2^- = Q\, A_2^+ \mathrm{e}^{-2\mathcal{H}L_I}, \tag{B 3}$$

where $Q = 0, \pm 1$ represent the infinite, capped, and open end conditions, respectively. It follows from Eqs. (B 1) and (B 3), that

$$\hat{p}_{1+} = A_2^+ + A_2^- = A_2^+(1 + Q\mathrm{e}^{-2\mathcal{H}L_I}), \tag{B 4a}$$

$$\frac{\mathrm{d}\hat{p}_{1+}}{\mathrm{d}x} = -\mathcal{H}\left(A_2^+ - A_2^-\right) = -\mathcal{H}A_2^+\left(1 - Q\mathrm{e}^{-2\mathcal{H}L_I}\right). \tag{B 4b}$$

2. First Segment

The transfer function $\hat{p}_1/\hat{p}_0$ can now be determined by considering the conditions on the pressure and its streamwise derivative at the exit of the first segment. From Eq. (B 1), it follows that

$$\hat{p}_{1-} = A_1^+ \mathrm{e}^{-\mathcal{H}L_S} + A_1^- \mathrm{e}^{\mathcal{H}L_S}, \tag{B 5a}$$

$$\frac{\mathrm{d}\hat{p}_{1-}}{\mathrm{d}x} = -\mathcal{H}\left(A_1^+ \mathrm{e}^{-\mathcal{H}L_S} - A_1^- \mathrm{e}^{\mathcal{H}L_S}\right). \tag{B 5b}$$

Combining Eqs. (B 4a) and (B 5a) produces

$$A_1^+ \mathrm{e}^{-\mathcal{H}L_S} + A_1^- \mathrm{e}^{\mathcal{H}L_S} = A_2^+(1 + Q\mathrm{e}^{-2\mathcal{H}L_I}). \tag{B 6}$$

Substituting Eqs. (B 4b) and (B 5b) into Eq. (A 12) yields

$$A_1^+ \mathrm{e}^{-\mathcal{H}L_S} - A_1^- \mathrm{e}^{\mathcal{H}L_S} - A_2^+ \left(1 - Q\mathrm{e}^{-2\mathcal{H}L_I}\right) = \frac{\gamma V_T}{n_T \pi r_o^2 \mathcal{H}} \left(\frac{\omega}{c_o}\right)^2 \frac{J_0(\alpha)}{J_2(\alpha)} \hat{p}_1 \,. \tag{B 7}$$

Combining these two equations produces

$$\frac{A_1^+ \mathrm{e}^{-\mathcal{H}L_S} Q\mathrm{e}^{-2\mathcal{H}L_I}}{1 + Q\mathrm{e}^{-2\mathcal{H}L_I}} - \frac{A_1^- \mathrm{e}^{\mathcal{H}L_S}}{1 + Q\mathrm{e}^{-2\mathcal{H}L_I}} = \frac{\gamma V_T}{n_T 2\pi r_o^2 \mathcal{H}} \left(\frac{\omega}{c_o}\right)^2 \frac{J_0(\alpha)}{J_2(\alpha)} \hat{p}_1 \,. \tag{B 8}$$

Substituting Eq. (B 2), for $j = 1$, into this result and rearranging terms, produces the following result for the transfer function:

$$H(f) \equiv \frac{\hat{p}_1}{\hat{p}_0} = \mathrm{e}^{-\mathcal{H}L_S} \left[\frac{1 + Q\mathrm{e}^{-2\mathcal{H}(L_S+L_I)}}{1 + Q\mathrm{e}^{-2\mathcal{H}L_I}} + \frac{\gamma V_T}{n_T 2\pi r_o^2 \mathcal{H}} \left(\frac{\omega}{c_o}\right)^2 \frac{J_0(\alpha)}{J_2(\alpha)} \left(1 - \mathrm{e}^{-2\mathcal{H}L_S}\right) \right]^{-1} . \tag{B 9}$$

Note that $V_T f / \pi r_o^2 c_o$ represents the ratio of the transducer volume to the volume in the line corresponding to the acoustic wavelength of the perturbation motion and can be expected to be rather small for the cases studied in this report. Since both γ / n_T and $|\mathcal{H}| c_o / \omega$ can be expected to be of order unity, one could be led to believe that the term involving V_T in Eq. (B 9) could be neglected without any significant loss of accuracy. However, this is only true for cases where $Q \neq 0$ and L_I has a finite value. For sufficiently long, or perfectly terminated, lines, the transducer volume, V_T, needs to be accounted for in predictions.

3. Large-Shear-Number Limit

Equation (B 9) is the general results for the ITP under consideration here. For large shear numbers, i.e. $W >> 1$, it reduces to

$$H(f) \approx \mathrm{e}^{-\mathcal{H}L_S} \left\{ \frac{1 + Q\mathrm{e}^{-2\mathcal{H}(L_S+L_I)}}{1 + Q\mathrm{e}^{-2\mathcal{H}L_I}} - \mathrm{i} \frac{\gamma V_T}{n_T 2\pi r_o^2} \left(\frac{\omega}{c_o}\right) \left[1 + \frac{1 + \mathrm{i}}{\sqrt{2} W} \left(1 - \frac{\gamma - 1}{\sqrt{\sigma}} \right) \right] \left(1 - \mathrm{e}^{-2\mathcal{H}L_S}\right) \right\}^{-1} , \tag{B 10}$$

where $\mathcal{H}$ is given by Eqs. (A 9) and (A 20). The large-shear-number result (B 10) further supports the importance of the transducer-volume effects except under certain conditions.

References

[1] Mongeau, L., Huff, D., and Tester, B. J., "Aircraft Noise Technology Review and Medium and Long Term Noise Reduction Goals," *ICA 2013 Montreal*, 2013. doi:10.1121/1.4800944.

[2] Dowling, A. P., and Mahmoudi, Y., "Combustion Noise," *Proceedings of the Combustion Institute*, Vol. 35, 2015, pp. 65–100.

[3] Ihme, M., "Combustion and Engine-Core Noise," *Annual Review of Fluid Mechanics*, Vol. 49, 2017, pp. 277–310.

[4] Minami, T., and Ahuja, K. K., "Five Microphone Method for Separating Two Different Noise Sources from Farfield Measurements Contaminated by Extraneous Noise," AIAA Paper 2003-3261, 9th AIAA/CEAS Aeroacoustic Conference, Hilton Head, South Carolina, 2003.

[5] Mendoza, J. M., Nance, D. K., and Ahuja, K. K., "Source Separation from Multiple Microphone Measurements in the Far Field of a Full Scale Aero Engine," AIAA Paper 2008-2809, 14th AIAA/CEAS Aeroacoustic Conference, Vancouver, British Columbia, 2008.

[6] Hultgren, L. S., and Miles, J. H., "Noise-Source Separation Using Internal and Far-Field Sensors for a Full-Scale Turbofan Engine," AIAA Paper 2009-3220 (NASA/TM–2009-215834), 15th AIAA/CEAS Aeroacoustic Conference, Miami, Florida, 2009.

[7] Hultgren, L. S., "Full-Scale Turbofan-Engine Turbine-Transfer Function Determination Using Three Internal Sensors," AIAA Paper 2011-2912 (NASA/TM-2012-217252), 17th AIAA/CEAS Aeroacoustic Conference, Portland, Oregon, 2011.

[8] Hultgren, L. S., and Arechiga, R. O., "Full-Scale Turbofan Engine Noise-Source Separation Using a Four-Signal Method," Tech. Rep. NASA/TM–2016-219419, NASA, 2016.

[9] Boyle, D. K., Henderson, B. S., and Hultgren, L. S., "Core/Combustor-Noise Baseline Measurements for the DGEN Aeropropulsion Research Turbofan," AIAA Paper 2018-3281, 24th AIAA/CEAS Aeroacoustics Conference, Atlanta, GA, 2018.

[10] Karchmer, A. M., and Reshotko, M., "Core Noise Source Diagnostics on a Turbofan Engine Using Correlation and Coherence Techniques," Tech. Rep. NASA-TM-X-73535, NASA, 1976.

[11] Weir, D. S., "Engine Validation of Noise and Emission Reduction Technology Phase I," Tech. Rep. NASA/CR-2008-215225, NASA, 2008. Honeywell Report No. 21-13843, Honeywell Aerospace, Phoenix, Arizona.

[12] Iberall, A. S., "Attenuation of Oscillatory Pressures in Instrument Lines," *J. Research National Bureau Standards*, Vol. 45, 1950, pp. 85–108.

[13] Bergh, H., and Tijdeman, H., "Theoretical and Experimental Results for the Dynamic Response of Pressure Measuring Systems," Tech. Rep. NLR-TR-F.238, Netherlands Aerospace Center (NLR), 1965.

[14] Samuelson, R. D., "Pneumatic Instrumentation Lines and Their Use in Measuring Rocket Nozzle Pressure," Tech. Rep. RN-DR-0124, Aerojet General Corporation, 1967.

[15] Hurst, A. M., Olsen, T. R., Goodman, S., VanDeWeert, J., and Shang, T., "An Experimental Frequency Response Characterization of MEMS Piezoresistive Pressure Transducers," Paper GT2014-27159, ASME Turbo Expo 2014, Düsseldorf, Germany, 2014. doi:10.1115/GT2014-27159.

[16] Abramowitz, M., and Stegun, I. A., *Handbook of Mathematical Functions with Formulas, Graphs, and Mathematical Tables*, 10th printing with corrections, United States Department of Commerce, National Bureau of Standards, 1972.